NJC

PAPER

View Article Online
View Journal | View Issue

Cite this: *New J. Chem.*, 2017, **41**, 15458

Highly stable and conductive PEDOT:PSS/graphene nanocomposites for biosensor applications in aqueous medium†

Dongtao Liu,‡[a] Md. Mahbubur Rahman,‡[b] Chuangye Ge,[a] Jaecheon Kim[a] and Jae-Joon Lee *[a]

Received 6th September 2017,
Accepted 6th November 2017

DOI: 10.1039/c7nj03330c

rsc.li/njc

In this article, we demonstrated the development of highly water-stable and conductive poly(3,4-ethylenedioxythiophene):poly(styrene sulfonate) (PEDOT:PSS)/graphene nanoplatelet (GNP) [PPG] composites on a fluorine-doped tin oxide (FTO) electrode for the detection of dopamine (DA) in the presence of ascorbic acid (AA) and uric acid (UA) in aqueous medium. PPG was deposited on FTO *via* the electrospray technique from a mixture solution of PEDOT:PSS and GNPs, which was subsequently treated with sulfuric acid (H_2SO_4, 98%). Acid treatment enabled stabilisation of the GNPs on FTO in water, due to the removal of insulating and hydrophilic PSS (68%) from the composites, and concurrently increased the conductivity (105 S cm^{-1}), owing to the presence of a high percentage of hydrophobic and conductive PEDOT, as well as strong $\pi-\pi$ interactions between PEDOT and GNPs. The untreated PPG electrode exhibited low water stability of GNPs and low conductivity (23 S cm^{-1}). Accordingly, the acid-treated PPG/FTO electrode showed very high electrochemical stability, low charge transfer resistance (R_{ct}) at the electrode|electrolyte interface, and improved catalytic activity for the oxidation of DA in aqueous buffer solution with very high sensitivity. It showed sufficiently high anodic peak-to-peak potential separations (ΔE_{pa}) between DA and AA (0.27 V) and DA and UA (0.11 V) for the interference-free detection of DA with a detection limit (S/N = 3) and sensitivity of ~105 nM and 27.7 μA μM^{-1} cm^{-2}, respectively.

1. Introduction

Graphene, a two-dimensional (2D) layered nanomaterial with sp^2-bonded carbon atoms in a honeycomb structure, has attracted significant interest from scientists and industries worldwide, due to its high surface area, outstanding conducting/semiconducting properties arising from the confinement of electrons in 2D, high charge-carrier mobility, and lateral dimension dependent physical, chemical, and mechanical properties.[1–5] Graphene has been utilised for the development of various technological devices that include solar cells, biosensors, energy and gas storage, and catalytic reactions.[6–9] However, the main challenge for the development of pure graphene electrode based technologies with a liquid system is its dissolution in liquid electrolytes from the substrate/current collector by chemical/physical interactions. This results in unstable and less-reproducible signals, and ultimately decreases the long-term durability of the devices.[10] In particular, water shows a strong wetting and swelling effect on a freshly cleaved graphene surface, and significantly decreases the contact angle, compared to the atmospherically aged graphene.[11] In addition, liquid-induced damage of graphene at its edges is also observed, when a droplet of the liquid electrolyte solution with ethylene-glycol, glycerol, and water as a solvent was introduced at its basal plane.[12,13] To increase the mechanical stability of graphene based electrodes in a liquid system, various non-conducting polymers (*e.g.* diphenylalanine, polyvinylpyrrolidone, polyurethane, polyolefin, and nafion)[10,14–17] have been used to develop polymer–graphene composites. However, these non-conducting polymer based graphene composites are highly likely to show poor electrochemical and catalytic properties, due to the insulating nature of polymers.

Thus, the development of graphene composite electrodes with high enough electrical conductivity and aqueous stability is required for the development of many electronic devices, particularly for electrochemical biosensors, which are often operated in an aqueous medium under physiological conditions to detect biologically meaningful markers. In this regard,

[a] *Department of Energy & Materials Engineering, Dongguk University, Seoul, 100-715, Korea. E-mail: jjlee@dongguk.edu*
[b] *Nanotechnology Research Center and Department of Applied Life Science, College of Biomedical and Health Science, Konkuk University, Chungju 380-701, Korea*

† Electronic supplementary information (ESI) available: Optical characterisation, SEM, XPS, CV, and EIS characterisation, and stability and reproducibility tests. See DOI: 10.1039/c7nj03330c

‡ Both the authors contributed equally.

the development of conducting polymer (CP)/graphene composites is an attractive approach to increase the stability of graphene-based electrodes in a liquid system, without sacrificing conductivity. To date, various CPs, including poly(aniline), poly(pyrrole), poly(thiophene), and poly(3,4-ethylenedioxythiophene):poly(styrenesulfonate) (PEDOT:PSS), have been used to develop electrodes of CP/graphene composites for various applications in aqueous systems.[18–21] Even though the stability of these composites in the liquid phase was not thoroughly investigated, the hydrophilic nature of most CPs may decrease the chemical/mechanical stability in aqueous electrolyte. Among CPs, PEDOT:PSS (PP) with a core–shell structure of hydrophobic and highly conductive PEDOT encapsulated by hydrophilic and insulating PSS can be an attractive choice to develop graphene composite electrodes with high liquid stability.[22] However, the significantly low conductivity of PP (<1 S cm^{-1}) and the hydrophilicity of PSS often caused a deterioration of the water stability of electrodes with PP-Graphene (PPG) composites, which resulted in poor electrical/electrochemical performance.[23] To increase the conductivity, treatment of PP electrodes with formic acid, sulfuric acid (H_2SO_4), hydroiodic acid (HI), and dimethylsulfoxide (DMSO) has been demonstrated, and it has been shown that the conductivity of PP electrodes could be significantly enhanced by reducing the amount of insulating PSS up to 60–70%.[21,24–27] Zhang *et al.* fabricated a H_2SO_4 post-treated PPG composite electrode, which exhibited significant enhancement of conductivity and electrocatalytic activity for the oxygen reduction reaction in aqueous medium.[21] A PPG composite based enzymatic glucose biosensor, fabricated by Wisitsoraat *et al.* without any pre- or post-treatment, showed relatively long-term stability (30% loss of the initial response) in detecting the glucose oxidation signal with successive measurements, when the electrode was stored under dry conditions.[28]

In this research, we developed a PPG electrode on fluorine-doped tin oxide (PPG/FTO) with high electrical conductivity, catalytic activity, and excellent water stability by H_2SO_4 post-treatment of PPGs prepared by electro-spraying a mixture solution of PP and graphene nano-platelets (GNPs) onto FTO. It was used as a sensor for detecting dopamine (DA, 3,4-dihydroxy phenylalanine) in the presence of ascorbic acid (AA) and uric acid (UA) in aqueous medium (phosphate buffer solution, PBS, pH 7.0). DA is a vitally important compound that exists in the human neural system as a neurotransmitter, and plays a major role in the human renal, central nervous, and cardiovascular systems. It has often been used as a target analyte for schizophrenia and Parkinson's, Alzheimer's, and cardiovascular diseases.[5,29] The acid-treated PPG/FTO sensor showed excellent catalytic activity and high sensitivity for the detection of DA in the presence of common interferences of AA and UA, with very high water stability and reproducibility.

2. Experimental

2.1. Reagents and materials

Graphene nanoplatelets (GNPs) were purchased from XG Sciences, Inc. (C-500, USA), with a particle diameter <2 μM and a surface area of ~ 500 m^2 g^{-1}. The carboxyl (–COO$^-$) functional groups and nitrogen dopant at the edges of the GNPs were ~ 5.5 and 1.5%, respectively.[5] Poly(3,4-ethylenedioxythiophene):poly(styrenesulfonate) (PEDOT:PSS) solution (1.3 wt% dispersion in water) was obtained from Sigma-Aldrich (St. Louis, MO, USA). Fluorine-doped tin oxide (FTO, Pilkington TEC Glass-TEC 8, Solar, 2.3 mm thickness) glass was used as the substrate. DA, AA, UA, disodium hydrogen phosphate (Na_2HPO_4), sodium dihydrogen phosphate (NaH_2PO_4), H_2SO_4 ($\sim 98\%$), α-D-glucose, sodium nitrate ($NaNO_3$), citric acid (CA) and potassium ferro/ferricyanide ($K_4[Fe(CN)_6]/K_3[Fe(CN)_6]$) were obtained from Sigma-Aldrich. PBS (pH 7.0), as a supporting electrolyte, was prepared by mixing 0.1 M $Na_2HPO_{4(aq)}$ and 0.1 M $NaH_2PO_{4(aq)}$. All of the chemicals were of analytical grade, and were used without any further purification. The normal human urine for real sample analysis was purchased from Innovative Research, USA.

2.2. Measurements and instrumentation

A general three-electrode system containing PPG, platinum (Pt), and Ag/AgCl as working, counter, and reference electrodes, respectively, was used to measure electrochemical signals on a CHI 430A electrochemical workstation (CH Instruments, USA). Electrochemical impedance spectra (EIS) were obtained on a VersaSTAT 3 electrochemical workstation (AMETEK Scientific Instruments, USA) in a mixture solution of $K_4[Fe(CN)_6]/K_3[Fe(CN)_6]$ (5 mM each) in the 10^{-1}–10^6 Hz frequency range with an AC amplitude of 5 mV. The EIS parameters were quantified by fitting the spectra with an appropriate equivalent circuit using Z-view software (Scribner Associates Inc., version 3.1). The binding energies of the samples were characterised using X-ray photoelectron spectroscopy (XPS, ULVAC-PHI, Japan). Scanning electron microscopy (SEM, JEOL-7100F, Japan) and optical microscopy (OLYMPUS, BX51M, Japan) were used to observe the morphologies of the electrodes. The conductivity was measured using a resistivity meter (Mitsubishi Chemical Analytech Co. Ltd, MCP-T610, Japan) with a four-point probe. The thicknesses of the electrodes were measured with a surface profiler (ACCRETECH, Surfcom 130A, Japan). Raman scattering spectra were recorded on a Raman spectrometer (Renishaw plc, RA802, UK) at an excitation wavelength of 532 nm.

2.3. Preparation of the electrodes

Prior to the preparation of electrodes, GNPs were ball milled for 24 h to decrease the aggregation of particles. 1 wt% of ball-milled GNPs was mixed with diluted PP (PP/EtOH = 1 : 3 v/v), and sonicated for 30 min. Then, the mixture solution was directly deposited onto an FTO substrate using an electro-spraying method. For comparison, pure GNPs (1 wt% dispersion in 2-propanol) and diluted PP (PP/EtOH = 1 : 3 v/v) were also deposited on FTO electrodes. E-spraying was performed by loading the solutions into a plastic syringe with a 27-gauge stainless steel hypodermic needle, which was connected to a high voltage power supply (ESN-HV30). A voltage of ~ 9.0 kV was applied between a metal orifice and the FTO substrate at a distance of 4.0 cm, as shown in Fig. S1 (ESI†). The injection rate was 50 μL min^{-1} with a deposition time of 2 min for PPG and

GNPs, and 6 min for PP. Then, the electrodes were dried at 80 °C in a vacuum drying oven for 30 min. The freshly prepared PPG and PP modified FTO electrodes (denoted as untreated PPG_{UT} and PP_{UT}) were immersed in concentrated H_2SO_4 (98%) for 3 h at 125 °C using a hot plate to remove the PSS from PPG and PP, and they are denoted as PPG_{AT} and PP_{AT}, respectively. The electrodes were rinsed with distilled water, and then dried at 80 °C for 30 min in a vacuum oven. Finally, PPG_{UT}, PP_{UT}, PPG_{AT}, and PP_{AT} were treated with water by immersing them in distilled water at 80 °C for 30 min, and they are denoted as PPG_{UT-WT}, PP_{UT-WT}, PPG_{AT-WT}, and PP_{AT-WT}, respectively. Similarly, pure GNP modified FTO electrodes without/with water treatment are denoted as GNP_{UT} and GNP_{WT}, respectively.

3. Results and discussion

3.1. Morphological characterisation

Fig. 1(a) shows an SEM image of GNP_{UT} deposited on FTO, which reveals a homogeneous distribution of GNPs with porous structures. After dipping GNP_{UT}/FTO in water, almost 100% of GNPs were detached from the FTO surface, as evidenced by the appearance of the FTO substrate only (Fig. 1(b)). This was further verified by observing their surface morphologies with low magnification using optical microscopy (Fig. S2(a) and (b), ESI†). The very weak adhesion of GNPs on the FTO substrate in water can be ascribed to the absence of any physical or chemical interactions of GNPs with FTO, as well as the possible chemical or hydrophilic interaction between the $-COO^-$ functional groups of GNPs and water.[30] Fig. 1(c) and (d) show SEM images of PPG_{UT}/FTO and PPG_{UT-WT}/FTO, respectively, which also reveal the substantial removal of GNPs from the FTO surface after water treatment, induced by hydrophilic PSS. However, the adhesion of GNPs to the FTO was increased in the presence of PP, which was again confirmed by their optical images (Fig. S2(c) and (d), ESI†, respectively). In contrast, PPG_{AT} and PPG_{AT-WT} do not reveal any noticeable changes in morphology (Fig. 1(e) and (f), respectively), indicating the high stability of GNPs on FTO in aqueous medium, which is consistent with the optical images (Fig. S2(e) and (f) (ESI†), respectively). In addition, we also analysed the surface morphologies of PP_{UT}, PP_{UT-WT}, PP_{AT}, and PP_{AT-WT} (Fig. S3 (a)–(d), ESI†, respectively), which displayed unaltered morphologies in both PP_{AT} and PP_{AT-WT}, with entangled wire-like structures due to the removal of PSS.[27]

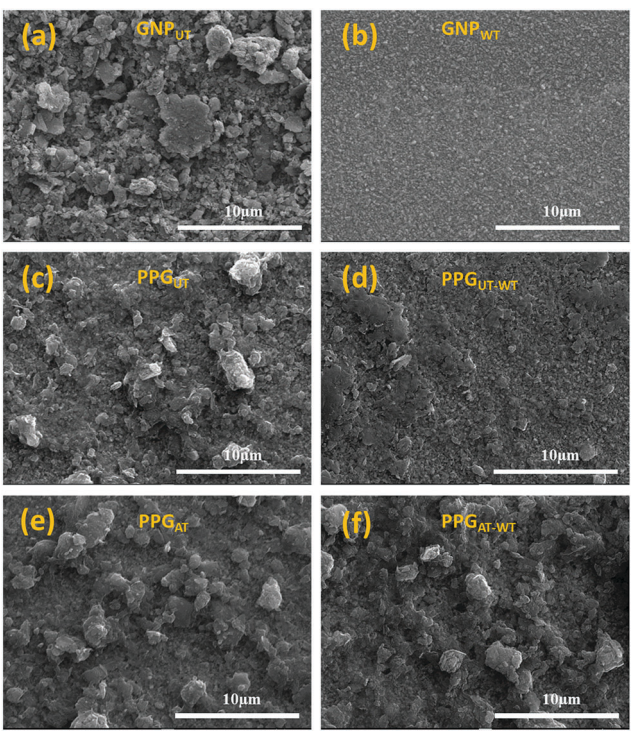

Fig. 1 Scanning electron microscopy (SEM) images of (a) GNP_{UT}, (b) GNP_{WT}, (c) PPG_{UT}, (d) PPG $_{UT-WT}$, (e) PPG_{AT}, and (f) PPG_{AT-WT}.

3.2. XPS characterisation

XPS was used to confirm the surface chemical states and compositions of PPG_{UT}, PPG_{AT}, and PPG_{AT-WT} samples. Fig. 2(a)–(c) show narrow band XPS spectra of S 2p for PPG_{UT}, PPG_{AT}, and PPG_{AT-WT}, respectively, while Fig. 2(d)–(f) show those of O 1s, respectively. Table 1 and Fig. S4 (ESI†) show the binding energies of all the peaks and survey XPS spectra, respectively. The core-level S $2p_{1/2}$ and S $2p_{3/2}$ peaks from the thiophene unit of PEDOT in PPG_{UT} were located at ~163.40 and 162.42 eV, respectively, while they were ~163.10 and 161.90 eV, respectively, for PPG_{AT}, and ~163.10 and 161.98 eV, respectively, for PPG_{AT-WT}.[31–33] On the other hand, the core-level XPS peaks of S $2p_{1/2}$ and S $2p_{3/2}$ from the sulfonate group ($-SO_3^-$) of PSS in PPG_{UT} were located at ~167.70 and 166.50 eV, respectively, while they were at ~166.20 and 164.95 eV, respectively, for PPG_{AT}, and ~166.43 and 165.30 eV, respectively, for PPG_{AT-WT}.[31–33] The S 2p peaks of both PEDOT and PSS in both PPG_{AT} and PPG_{AT-WT} shifted to lower binding energies, compared to the S 2p peaks in PPG_{UT}. This can be ascribed to the removal of PSS from the composite film after acid treatment, consistent with a

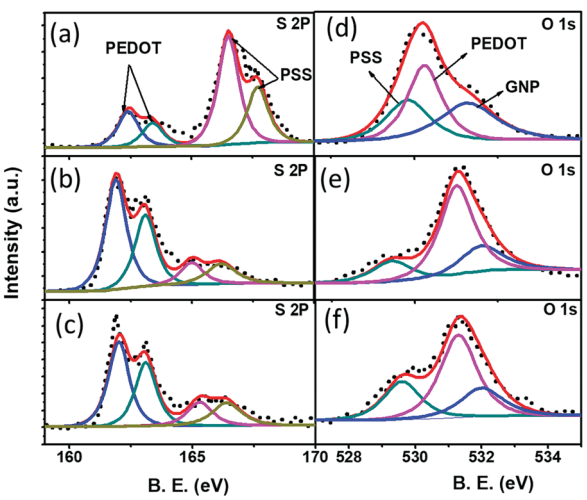

Fig. 2 X-ray photoelectron (XPS) narrow scan spectra of S 2p (a)–(c) for PPG_{UT}, PPG_{AT}, and PPG_{AT-WT}, respectively, and narrow scan spectra of O 1s (d)–(f) for PPG_{UT}, PPG_{AT}, and PPG_{AT-WT}, respectively. The dotted lines indicate the experimental data, while the solid lines denote the fitted curves.

Table 1 Binding energies of the S $2p_{1/2}$, S $2p_{3/2}$, and O 1s levels in XPS fitting

	PEDOT binding energy (eV)			PSS binding energy (eV)			GNP binding energy (eV)
Sample	S $2p_{1/2}$	S $2p_{3/2}$	O 1s (C–O–C)	S $2p_{1/2}$	S $2p_{3/2}$	O 1s (O═S)	O 1s (COO^-)
PPG_{UT}	163.40	162.42	530.30	167.70	166.50	529.80	531.61
PPG_{AT}	163.10	161.90	531.26	166.20	164.95	529.35	532.0
PPG_{AT-WT}	163.10	161.98	531.32	166.43	165.30	529.55	532.02
PP_{UT}	164.20	163.15	532.21	168.20	167.10	530.60	—
PP_{AT}	163.95	162.99	532.42	167.80	166.30	530.39	—

previous report.[24] Furthermore, the intensities of the S 2p peaks of PSS in both PPG_{AT} and PPG_{AT-WT} were significantly decreased compared to PPG_{UT}, which was consistent with the removal of PSS from the PPG film upon acid treatment. Meanwhile, the S 2p peak positions and intensities of both PEDOT and PSS in PPG_{AT-WT} were almost the same as those of the S 2p peaks of PPG_{AT}, and indicated the high water stability of PPG_{AT}. The ratio of PEDOT to PSS in PPG_{UT} was ~1 : 2.60, while it was ~1 : 0.83 and 1 : 0.80 in PPG_{AT} and PPG_{AT-WT}, respectively, which corresponds to ~68 and 70% removal of PSS from the PPG film after acid and subsequent water treatment, respectively. This small variation (2%) of PSS between the PPG_{AT} and PPG_{AT-WT} is possibly due to the additional removal of PSS from the PPG_{AT} upon water treatment.

The narrow band XPS spectra of O 1s in PPG_{UT} exhibited three core-level peaks located at ~529.80, 530.30, and 531.61 eV, which can be assigned to O═S, C–O–C, and $–COO^-$, for PSS, PEDOT, and GNPs, respectively.[32–35] Similarly, these three peaks were found at ~529.35, 531.26, and 532.0 eV, respectively, for PPG_{AT}, and at ~529.55, 531.32, and 532.02 eV, respectively, for PPG_{AT-WT}. The smaller binding energy for O═S peaks in PPG_{AT}, ~0.45 eV with respect to that of PPG_{UT}, might be attributed to the removal of PSS from the composite film, which was enabled by the formation of PSSH by reacting H^+ with PSS^-.[24] In contrast, the C–O–C and $–COO^-$ peaks for PEDOT and GNPs shifted to higher binding energies in both PPG_{AT} and PPG_{AT-WT}, without any noticeable changes in peak intensity and peak area. These indicated a stronger π–π interaction between PEDOT and GNPs, which could be attributed to an additional oxidative functionalisation of GNPs to form more $–COO^-$ by H_2SO_4.[21] The S 2p and O 1s core-level spectra (Fig. S5, ESI†) and survey spectra (Fig. S6, ESI†) of PP_{UT} and PP_{AT} also revealed similar trends in the intensity variation and peak shifting, which strongly support the removal of PSS from PP by H_2SO_4 treatment, and concurrent enhancement of the interaction between PEDOT and GNPs.

Fig. 3 shows a schematic of the removal of PSS from PPG that is induced by the formation of HSO_4^- and $H_3SO_4^+$ *via* autoprotolysis of concentrated H_2SO_4.[36] The positively charged $H_3SO_4^+$ ions (*i.e.* H^+) associate with the negatively charged PSS^- to form PSSH by the $H^+ + PSS^- \rightarrow$ PSSH reaction. This can be easily removed from the shell of PP by washing with water, due to the loss of coulombic interaction with the positively charged PEDOT, as well as its hydrophilicity,[25,26] whereas a little fraction of PSS^- remain with a positively charged PEDOT as a counter ion. This is consistent with the fact that the dissociation constant (pK_{a1}) of H_2SO_4 (−10) is much larger than that of the pK_a of PSSH (−2.8). Meanwhile, the positively charged and hydrophobic PEDOT was stabilised by negatively charged HSO_4^-.[25] During the removal of PSSH by sufficient water washing, the HSO_4^- that electrostatically interacted could be easily removed from the PEDOT. Then, strong π–π stacking interactions between the rigid PEDOT molecules themselves, and between PEDOT and GNPs, induced significant changes in the morphological and crystallographic

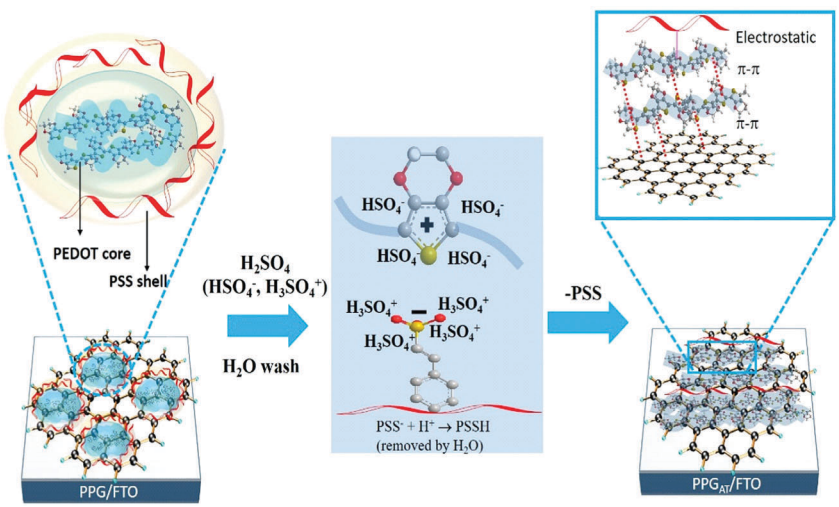

Fig. 3 Schematic of the removal of PSS from the PPG by H_2SO_4 treatment.

structures, *via* the formation of entangled wire-like structures, and thus stabilised PPG_{AT} in aqueous medium.[21,37,38]

3.3. Electrochemical characterisation and stability

Fig. 4(a) shows the CVs of PPG_{UT}/FTO and PPG_{AT}/FTO electrodes for $[Fe(CN)_6]^{3-/4-}$ at a scan rate of 100 mV s^{-1} in the potential range from −0.3 to +0.7 V, while Fig. S7 (ESI†) shows the corresponding CVs for GNP_{UT}/FTO, PP_{UT}/FTO, and PP_{AT}/FTO. The PPG_{AT}/FTO showed the highest value of oxidation peak current (I_{pa}), and the most reversible behavior for the $[Fe(CN)_6]^{3-/4-}$ redox couple among the electrodes, with an I_{pa} of 1 mA cm^{-2}; while the I_{pa} values for PPG_{UT}/FTO, GNP_{UT}/FTO, PP_{UT}/FTO, and PP_{AT}/FTO were ∼0.775, 0.414, 0.785, and 0.90 mA cm^{-2}, respectively. The peak-to-peak potential separation (ΔE_p) for $[Fe(CN)_6]^{3-/4-}$ was ∼0.126 V at PPG_{AT}/FTO, whereas it was ∼0.25, 0.40, 0.26, and 0.13 V at PPG_{UT}/FTO, GNP_{UT}/FTO, PP_{UT}/FTO, and PP_{AT}/FTO, respectively. Apparently, the acid treated electrodes including PPG_{AT}/FTO and PP_{AT}/FTO showed better electrochemical performance, compared to the corresponding untreated counterparts, upon removal of the insulating PSS from the electrodes. The highest catalytic activity for PPG_{AT}/FTO can be ascribed to the intermolecular π–π stacking interaction between GNPs and PEDOT, which brings the additional electron by the positively charged PEDOT backbone with an electron withdrawing ability, and creates a net positive charge at the C atom of the GNP, while concurrently enhancing the carrier mobility and conductivity of the electrode.[39,40] The conductivities for PPG_{AT}/FTO, PPG_{UT}/FTO, PP_{UT}/FTO, and PP_{AT}/FTO were ∼105, 23, 0.7, and 37 S cm^{-1} and the thicknesses of PPG_{AT}, PPG_{UT}, PP_{UT}, and PP_{AT} films were ∼1.0, 1.22, 1.14, and 0.96 μm, respectively. The significantly low electrocatalytic activity of GNP_{UT} with a thickness of ∼0.76 μm might be attributed to its instability on the FTO surface in the aqueous $[Fe(CN)_6]^{3-/4-}$ system, in which the interconnections between GNPs and GNPs and GNPs and FTO were significantly weakened, to result in a concurrent decrease of electrical conductivity (1.4 S cm^{-1}). The additional oxidation of GNPs induced by ball milling can be another reason for low conductivity, which was confirmed using Raman spectroscopy (Fig. S8, ESI†). The peak intensity ratio of the D to G band (I_D/I_G) was increased from ∼0.75 to 0.84 after ball milling. This indicates that ball milling can produce a high level of defects with the oxygen-containing functional groups in the GNPs.

Fig. 4(b) shows the Nyquist plots of PPG_{UT}/FTO and PPG_{AT}/FTO for the $[Fe(CN)_6]^{3-/4-}$ redox couple. The charge transfer resistances (R_{ct}) at the electrode|electrolyte interface in PPG_{AT}/FTO and PPG_{UT}/FTO were ∼54.8 and 190.2 Ω. The significant decrease in R_{ct} in PPG_{AT}/FTO compared to PPG_{UT}/FTO further indicates the better catalytic activity of the acid treated electrode, and this is consistent with the CV results and conductivity data.

The electrochemical stabilities of the PPG_{UT}/FTO and PPG_{AT}/FTO electrodes were investigated by consecutive CV and EIS measurements in the aqueous $[Fe(CN)_6]^{3-/4-}$ redox couple. The EIS was measured after performing 10 consecutive CV sweeps in aqueous $[Fe(CN)_6]^{3-/4-}$ at a scan rate of 100 mV s^{-1}. Fig. 4(c) and (d) show the summary of CV and EIS parameters (I_{pa} and R_{ct}), while Fig. S9 (ESI†) shows the corresponding CV and EIS plots. The relative standard deviation (RSD) for the variation of I_{pa} with the consecutive CV cycles for PPG_{UT}/FTO

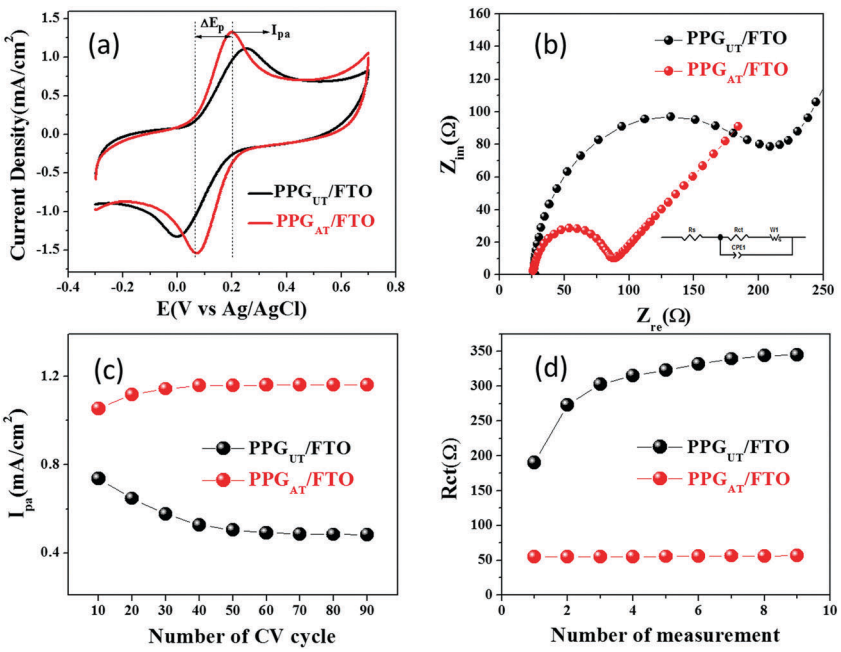

Fig. 4 (a) CVs (scan rate 100 mV s^{-1}), and (b) EIS plots for PPG_{UT}/FTO and PPG_{AT}/FTO electrodes in PBS (pH 7.0) containing $[Fe(CN)_6]^{3-/4-}$ (5 mM each). The inset of (b) shows the equivalent circuit model to fit the EIS plots. Variation of the (c) I_{pa} with the number of CV cycles (scan rate 100 mV s^{-1}), and (d) R_{ct} with the number of EIS measurements for the $[Fe(CN)_6]^{3-/4-}$ redox couple for PPG_{UT}/FTO and PPG_{AT}/FTO electrodes. The sequence of EIS measurements was as follows: 10× CV scans (potential range between −0.3 and +0.7 V, scan rate 100 mV s^{-1}); relaxation at 0 V (60 s); applied potential +0.3 V. This sequence of electrochemical stability testing was repeated 9 times.

was ~16.30%, while for PPG_{AT}/FTO it was ~3.12%. Meanwhile, the RSDs of R_{ct} variation for PPG_{UT}/FTO and PPG_{AT}/FTO were ~16.12 and 1.20%, respectively, which agree well with the trend of the I_{pa} variation.

3.4. Electrochemical responses of DA, UA, and AA at PPG_{AT}/FTO

Considering the physiological pH, PBS (pH 7.0) was chosen for the electrochemical detection of DA in the presence of AA and UA. Fig. 5(a) shows the CVs of a mixture solution of AA, DA, and UA (1 mM each, in PBS, pH 7.0) for the PPG_{UT}/FTO and PPG_{AT}/FTO electrodes. Both electrodes could separate the redox peaks of AA, DA, and UA from the mixture solution, while for all the analytes the sensitivity of PPG_{AT}/FTO was much higher than that of PPG_{UT}/FTO. The I_{pa} for DA was ~1.84 and 1.46 mA cm^{-2}, respectively, for PPG_{AT}/FTO and PPG_{UT}/FTO. Furthermore, the negative shifts of the oxidation peak potentials (E_{pa}) of all the analytes at PPG_{AT}/FTO compared to PPG_{UT}/FTO indicate the higher catalytic activity of PPG_{AT}/FTO than PPG_{UT}/FTO.[41,42] The enhanced catalytic activity and sensitivity of PPG_{AT}/FTO for DA oxidation can be attributed to the aromatic π–π stacking interaction between GNPs and DA, the cation–π interaction between the $-NH_3^+$ of DA (at pH 7.0) and the π electron of the benzene ring in GNPs, and the improved H-bonding interaction between the –OH group of DA and the oxygen functional groups of GNPs (*e.g.* $-COO^-$).[5] Meanwhile, PP in the PPG_{AT}/FTO can serve as a binder to stabilize GNPs, which also increase the charge transfer kinetics of DA oxidation by increasing the net positive charges in the C atom of the GNPs in PPG_{AT}, enabled by their positively charged backbones.[21] The E_{pa} values for AA, DA, and UA were about −0.05, 0.22, and 0.33 V, respectively, at PPG_{UT}/FTO, while they were about −0.09, 0.19, and 0.30 V, respectively, at PPG_{AT}/FTO. This is consistent with the improved sensitivity and catalytic activity observed for each analyte at PPG_{AT}/FTO in the individual solutions of AA, DA, and UA in PBS (pH 7.0) (Fig. S10, ESI†). The ΔE_{pa} values between AA and DA and DA and UA for PPG_{AT}/FTO were about 0.10 and 0.11 V, respectively, which are sufficient for the interference-free detection of DA from AA and UA. The inset of Fig. 5(a) shows the plot of I_{pa} *vs.* (scan rate)$^{1/2}$, which was obtained from the CVs of DA for the PPG_{AT}/FTO electrode with varying scan rates (Fig. S11, ESI†). The I_{pa} was directly proportional to the square root of the scan rates with a regression coefficient (R^2) of 0.994, and suggested a diffusion-controlled oxidation process of DA for PPG_{AT}/FTO.[29,42]

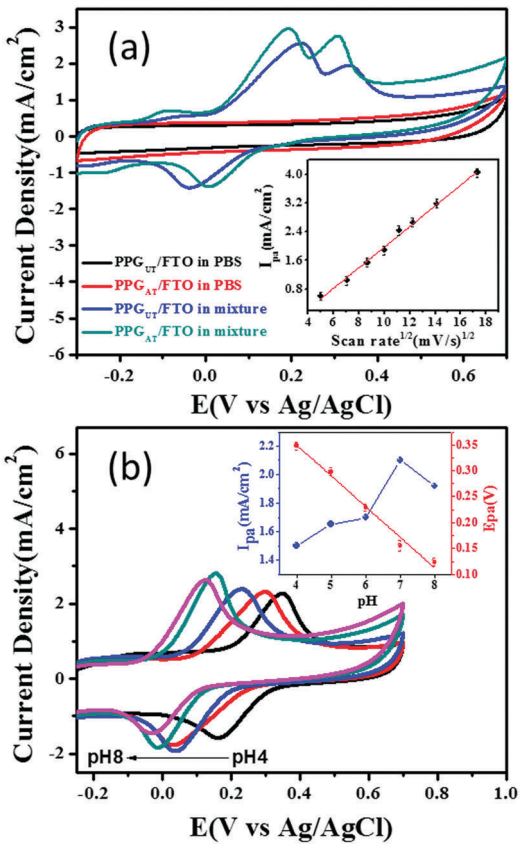

Fig. 5 (a) CVs of PPG_{UT}/FTO and PPG_{AT}/FTO electrodes in PBS (pH 7.0), and in a mixture solution of AA, DA, and UA (1 mM each in PBS, pH 7.0); scan rate 100 mV s^{-1}. The inset shows the plot of I_{pa} *vs.* (scan rate)$^{1/2}$. (b) CV responses of 1 mM DA for PPG_{AT}/FTO in the pH range from 4 to 8 at a scan rate of 100 mV s^{-1}. The inset shows the plots of I_{pa} *vs.* pH and E_{pa} *vs.* pH.

Fig. 5(b) shows the effect of pH on the oxidation of DA for PPG_{AT}/FTO. The E_{pa} was negatively shifted with the pH from 4 to 8, due to the different charging states of DA at different pH values,[5] similar to previous studies, where protons were involved in the redox reaction of DA.[43,44] The linear regression equation of the plot of E_{pa} *vs.* pH for the oxidation of DA was E_{pa} (mV) = −59.1 mV per pH + 585 (R^2 = 0.990). This corresponds to a slope of −59.1 mV per pH, close to a theoretical value of −59 mV per pH predicted from the Nernst equation,[43,44] specifying that the same ratio between electrons and protons was involved in the redox reaction of DA, which was two electrons to two protons. The I_{pa} for DA oxidation was the highest at pH 7.0, which is in accordance with the enhanced static interaction between DA and PPG_{AT}, and was considered as the optimal pH for further analysis.

3.5. Determination of DA in the presence of AA and UA

The selective and interference-free determination of DA at the PPG_{AT}/FTO sensor was studied using the differential pulse voltammetry (DPV) method in the presence of constant concentrations of AA (2 mM) and UA (30 μM), and varying concentrations of DA (1 to 30 μM) in PBS (pH 7.0), and Fig. 6(a) summarises the results. The I_{pa} of DA linearly increased with concentration (inset of Fig. 6a), while the I_{pa} values of both AA and UA remained constant. This corresponds to the linear regression equation of I_{pa} (μA cm^{-2}) = 27.7 × [DA]/(μM) + 29.0 (R^2 = 0.996) with a detection limit (S/N = 3) and sensitivity of ~105 nM and 27.7 μA (μM^{-1} cm^{-2}), respectively. The significantly low detection limit and high sensitivity for DA at PPG_{AT}/FTO are better than or comparable with many other reported DA sensors based on different nanocomposite modified electrodes (Table S1, ESI†). Similarly, the I_{pa} of UA at PPG_{AT}/FTO linearly increased with concentration (1 to 30) μM in the presence of constant concentrations of AA (2 mM) and DA

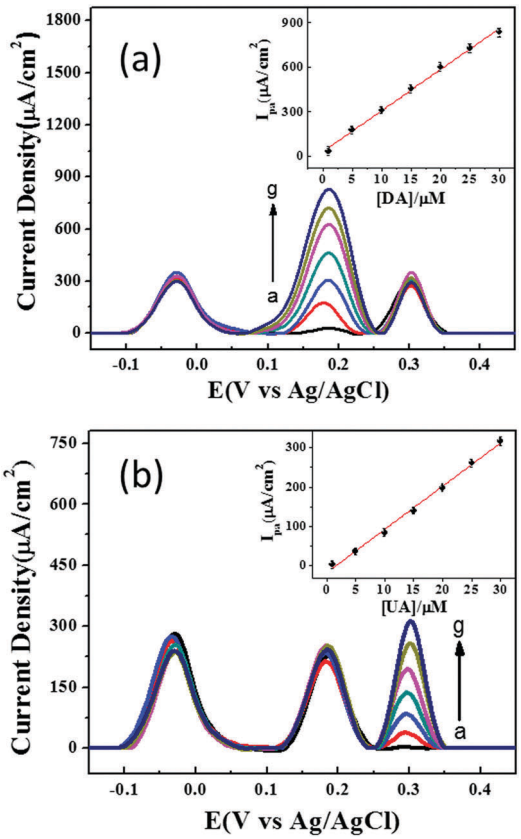

Fig. 6 (a) DPV responses of DA with varying concentrations (a → g: 1, 5, 10, 15, 20, 25, and 30 μM) in PBS (pH 7.0) for the PPG_{AT}/FTO sensor, in the presence of constant concentrations of AA (2 mM) and UA (30 μM). The inset shows the plot of I_{pa} *vs.* [DA]. (b) DPV responses of UA with varying concentrations (a → g: 1, 5, 10, 15, 20, 25, and 30 μM) in PBS (pH 7.0) for the PPG_{AT}/FTO sensor, in the presence of constant concentrations of AA (2 mM) and DA (10 μM). The inset shows the plot of I_{pa} *vs.* [UA]. DPV was obtained by scanning the potential with a pulse amplitude, pulse width, and pulse period of 100 mV s^{-1}, 2 ms, and 100 ms, respectively.

(10 μM) (Fig. 6(b)) with the linear regression equation I_{pa} (μA cm^{-2}) = 11.0 × [UA]/(μM) − 18.1 (R^2 = 0.996). This corresponds to a detection limit (S/N = 3) and sensitivity of ∼288 nM and 11.0 μA μM^{-1} cm^{-2}, respectively.

3.6. Stability, reproducibility, interference, and real sample analysis

The electrochemical stability of the PPG_{AT}/FTO sensor was examined by measuring the CV responses of DA (1 mM) for 10 consecutive cycles. This revealed a very low RSD of I_{pa} (1.12%) (Fig. S12(a), ESI†). The reproducibility of the sensor was tested by measuring the DPV responses of DA oxidation (30 μM) for three different PPG_{AT}/FTO sensors in the presence of AA (2 mM) and UA (30 μM) (Fig. S12(b), ESI†). The RSD for the I_{pa} of DA, ∼0.90%, indicated the excellent reproducibility of this sensor system. The PPG_{AT}/FTO sensor did not exhibit any noticeable variation in the I_{pa} of DA and UA in a mixture solution of DA and UA (30 μM each) in the absence and presence of AA (2 mM), glucose (1 mM), $NaNO_3$ (1 mM) and CA (1 mM) (Fig. S13, ESI†). The RSDs for the I_{pa} of DA in the presence of different interferences were only 2.0%, while it was 2.2% for UA.

Table 2 Estimation of DA in diluted human urine samples

Sample	Spiked (μM)	Found[a] (μM)	Recovery (%)
1	10	9.9	99.8
2	20	19.3	96.4
3	30	29.1	97.1

[a] Average of three measurements.

The feasibility of the PPG_{AT}/FTO sensor for practical application was investigated by measuring the concentrations of DA in human urine samples based on the standard addition method. The urine samples were diluted 100 times by adding PBS (pH 7.0), and different concentrations of DA were spiked in the samples. Table 2 summarizes the recovery results of spiked DA concentrations for the PPG_{AT}/FTO sensor obtained from DPV measurements and calibration plots. The excellent recoveries of DA, up to ∼96–99%, demonstrate the suitability of this sensor system for practical applications.

4. Conclusion

In summary, we have developed a H_2SO_4-treated PEDOT:PSS/graphene composite (PPG_{AT}) modified FTO electrode for dopamine (DA) sensing in aqueous medium. The PPG_{AT}/FTO electrode showed enhanced stability of GNPs on FTO in water with high conductivity and catalytic activity, and a low value of charge transfer resistance (R_{ct}) at the electrode|electrolyte interface. The enhanced stability and conductivity in the aqueous medium was attributed to the removal of hydrophilic and insulating PSS (up to ∼70%) to maintain a higher percentage of hydrophobic and conducting PEDOT, which showed a strong π–π interaction with GNPs. The PPG_{AT}/FTO electrode showed very high catalytic activity for DA detection in the presence of AA and UA, and it easily differentiated their electrochemical oxidation signals. The very high sensitivity and nanomolar-level detection limit with high stability and excellent recovery ratios from real sample analysis strongly suggest that the PPG_{AT}/FTO electrode is favorable for developing a disposable and cost-effective sensor for the real-time monitoring of DA. We believe that this water stable and highly electrocatalytic electrode system can be extended to the detection of various environmentally hazardous materials in an aqueous medium.

Conflicts of interest

There are no conflicts to declare.

Acknowledgements

This research was supported by the Basic Science Research Program through the National Research Foundation of Korea (NRF), funded by the Ministry of Education (NRF-2015M1A2A2054996, NRF-2016R1A2B2012061). It was also supported by the Technology Development Program to Solve Climate Changes of the National

Research Foundation (NRF), funded by the Ministry of Science, ICT & Future Planning (NRF-2016M1A2A2940912). This work was also supported by the Dongguk University Research Fund of 2016.

References

1 K. S. Novoselov, A. K. Geim, S. V. Morozov, D. Jiang, Y. Zhang, S. V. Dubonos, I. V. Grigorieva and A. A. Firsov, *Science*, 2004, **306**, 666–669.
2 A. K. Geim and K. S. Novoselov, *Nat. Mater.*, 2007, **6**, 183–191.
3 P. Bollella, G. Fusco, C. Tortolini, G. Sanzo, G. Favero, L. Gorton and R. Antiochia, *Biosens. Bioelectron.*, 2017, **89**, 152–166.
4 K. S. Novoselov, V. I. Fal'ko, L. Colombo, P. R. Gellert, M. G. Schwab and K. Kim, *Nature*, 2012, **490**, 192–200.
5 M. M. Rahman, N. S. Lopa, M. J. Ju and J.-J. Lee, *J. Electroanal. Chem.*, 2017, **792**, 54–60.
6 Y. Zhang, H. Li, L. Kuo, P. Dong and F. Yan, *Curr. Opin. Colloid Interface Sci.*, 2015, **20**, 406–415.
7 Y. Shao, J. Wang, H. Wu, J. Liu, I. A. Aksay and Y. Lin, *Electroanalysis*, 2010, **22**, 1027–1036.
8 C. H. Ng, H. N. Lim, S. Hayase, I. Harrison, A. Pandikumar and N. M. Huang, *J. Power Sources*, 2015, **296**, 169–185.
9 C.-H. Kim, H. Hlaing and I. Kymissis, *Org. Electron.*, 2016, **36**, 45–49.
10 K. Ryan, S. M. Neumayer, H. V. R. Maraka, N. V. Buchete, A. L. Kholkin, J. H. Rice and B. J. Rodriguez, *Sci. Technol. Adv. Mater.*, 2017, **18**, 172–179.
11 M. Velický, A. J. Cooper, P. S. Toth, H. V. Patten, C. R. Woods, K. S. Novoselov and R. A. W. Dryfe, *2D Mater.*, 2015, **2**, 024011.
12 P. S. Toth, A. T. Valota, M. Velický, I. A. Kinloch, K. S. Novoselov, E. W. Hill and R. A. W. Dryfe, *Chem. Sci.*, 2014, **5**, 582–589.
13 M. Velický, D. F. Bradley, A. J. Cooper, E. W. Hill, I. A. Kinloch, A. Mishchenko, K. S. Novoselov, H. V. Patten, P. S. Toth, A. T. Valota, S. D. Worrall and R. A. W. Dryfe, *ACS Nano*, 2014, **8**, 10089–10100.
14 S. Salgın, S. Takaç and T. H. Özdamar, *J. Membr. Sci.*, 2006, **278**, 251–260.
15 Y. Li, H. Lian, Y. Hu, W. Chang, X. Cui and Y. Liu, *Polymers*, 2016, **8**, 236.
16 S. N. Tripathi, G. S. S. Rao, A. B. Mathur and R. Jasra, *RSC Adv.*, 2017, **7**, 23615–23632.
17 S.-J. Li, J.-Z. He, M.-J. Zhang, R.-X. Zhang, X.-L. Lv, S.-H. Li and H. Pang, *Electrochim. Acta*, 2013, **102**, 58–65.
18 J. Yan, T. Wei, B. Shao, Z. Fan, W. Qian, M. Zhang and F. Wei, *Carbon*, 2010, **48**, 487–493.
19 L. Wang, F. Liu, C. Jin, T. Zhang and Q. Yin, *RSC Adv.*, 2014, **4**, 46187–46193.
20 C. Bora, C. Sarkar, K. J. Mohan and S. Dolui, *Electrochim. Acta*, 2015, **157**, 225–231.
21 M. Zhang, W. Yuan, B. Yao, C. Li and G. Shi, *ACS Appl. Mater. Interfaces*, 2014, **6**, 3587–3593.
22 L. Groenendaal, F. Jonas, D. Freitag, H. Pielartzik and J. R. Reynolds, *Adv. Mater.*, 2000, **12**, 481–494.
23 G.-H. Jeong, S.-J. Kim, H.-S. Ko, E.-M. Han and K. H. Park, *Mol. Cryst. Liq. Cryst.*, 2015, **620**, 117–122.
24 D. A. Mengistie, M. A. Ibrahem, P. C. Wang and C. W. Chu, *ACS Appl. Mater. Interfaces*, 2014, **6**, 2292–2299.
25 N. Kim, S. Kee, S. H. Lee, B. H. Lee, Y. H. Kahng, Y. R. Jo, B. J. Kim and K. Lee, *Adv. Mater.*, 2014, **26**, 2268–2272.
26 A. K. Sarker, J. Kim, B.-H. Wee, H.-J. Song, Y. Lee, J.-D. Hong and C. Lee, *RSC Adv.*, 2015, **5**, 52019–52025.
27 T.-R. Chou, S.-H. Chen, Y.-T. Chiang, Y.-T. Lin and C.-Y. Chao, *J. Mater. Chem. C*, 2015, **3**, 3760–3766.
28 A. Wisitsoraat, S. Pakapongpan, C. Sriprachuabwong, D. Phokharatkul, P. Sritongkham, T. Lomas and A. Tuantranont, *J. Electroanal. Chem.*, 2013, **704**, 208–213.
29 X.-B. Li, M. M. Rahman, G.-R. Xu and J.-J. Lee, *Electrochim. Acta*, 2015, **173**, 440–447.
30 V. Georgakilas, J. N. Tiwari, K. C. Kemp, J. A. Perman, A. B. Bourlinos, K. S. Kim and R. Zboril, *Chem. Rev.*, 2016, **116**, 5464–5519.
31 E. J. Bae, Y. H. Kang, K. S. Jang and S. Y. Cho, *Sci. Rep.*, 2016, **6**, 18805.
32 X. Wu, L. Lian, S. Yang and G. He, *J. Mater. Chem. C*, 2016, **4**, 8528–8534.
33 A. A. Farah, S. A. Rutledge, A. Schaarschmidt, R. Lai, J. P. Freedman and A. S. Helmy, *J. Appl. Phys.*, 2012, **112**, 113709.
34 J. W. Burress, S. Gadipelli, J. Ford, J. M. Simmons, W. Zhou and T. Yildirim, *Angew. Chem., Int. Ed.*, 2010, **49**, 8902–8904.
35 H. Yan and H. Okuzaki, *Synth. Met.*, 2009, **159**, 2225–2228.
36 N. N. Greenwood and A. Earnshaw, *Chemistry of the Elements*, Butterworth-Heinemann, Oxford, 1997.
37 N. Kim, B. H. Lee, D. Choi, G. Kim, H. Kim, J. R. Kim, J. Lee, Y. H. Kahng and K. Lee, *Phys. Rev. Lett.*, 2012, **109**, 106405.
38 E.-G. Kim and J.-L. Brédas, *J. Am. Chem. Soc.*, 2008, **130**, 16880–16889.
39 S. Wang, D. Yu and L. Dai, *J. Am. Chem. Soc.*, 2011, **133**, 5182–5185.
40 S. Wang, D. Yu, L. Dai, D. W. Chang and J.-B. Baek, *ACS Nano*, 2011, **5**, 6202–6209.
41 M. M. Rahman, N. S. Lopa, K. Kim and J.-J. Lee, *J. Electrochem. Soc.*, 2015, **162**, B159–B162.
42 Y. Liu, H.-L. Zhang, G.-S. Lai, A.-M. Yu, Y.-M. Huang and D.-Y. Han, *Electroanalysis*, 2010, **22**, 1725–1732.
43 H. R. Zare and S. M. Golabi, *J. Electroanal. Chem.*, 1999, **464**, 14–23.
44 L. Han and X. Zhang, *Electroanalysis*, 2009, **21**, 124–129.